EAI Endorsed Transactions
on Energy Web

Research Article EAI.EU

Robust Stability Control Theory and Characteristics Analysis of Networked Energy Storage Converters under Large Disturbance Scenarios

Fengshun Jiao[1*], Guoxing Wu[1], Weijie Gao[1], Chuyun She[1]

[1]Shenzhen Power Supply Co., Ltd., Shenzhen 518000, Guangdong, China

Abstract

INTRODUCTION: Grid-Forming Energy Storage Converter (GFM-ESC) is a key interface equipment for the coordinated regulation of source and network in new power systems. However, the dynamic coupling mechanism between its multi-topology structures such as direct-mounted, string-type, and centralized types and large disturbance scenarios (new energy power fluctuations, power grid transient shocks) has not yet been clarified.
OBJECTIVES: Existing robust control methods do not embed topological feature constraints and are difficult to ensure the system stability margin under large disturbances under multi-topology. This theoretical gap limits the scene adaptability of GFM-ESC. In response to the above scientific issues, this paper focuses on *Robust Stability Control Theory and Characteristics Analysis of Networked Energy Storage Converters under Large Disturbance Scenarios*.
METHODS: First, a large disturbance dynamic model of multi-topology GFM-ESC was established. By analyzing the mapping relationship among wiring topology, component parameters and system state matrix, the energy flow mechanism and eigenvalue trajectory instability inducements of GFM-ESC under different topologies were revealed during large disturbances, and the influence of topological parameters on the system was quantified. Secondly, grounded on H∞ robust control theory, a robust stable control method for topology adaptation was proposed, a closed-loop control law embedded with topological features was derived, and Lyapunov stability theory was used to prove the robust convergence of this control method under large disturbances and topological parameter perturbation scenarios. Finally, through small signal analysis and large disturbance numerical simulation, the performance of the developed theory and method was verified.
RESULTS: Findings showed that the developed dynamic model can accurately describe the large disturbance characteristics of multi-topology GFM-ESC, and the corresponding robust control method can increase the system stability margin by 42%, and can still maintain the asymptotic stability of the closed-loop system when the topological parameters were perturbed by 15%.
CONCLUSION: The results of this study enhance the theoretical system for controlling large disturbances in the multi-topology GFM-ESC, providing a foundation for the collaborative design of GFM-ESC topologies in new power systems.

Keywords: Grid-forming energy storage converter, Large disturbance scenario, Stability control, Dynamic model

Received on 14 August 2026, accepted on 27 October 2026, published on 09 November 2026

Copyright © 2026 Fengshun Jiao *et al.*, licensed to EAI. This is an open access article distributed under the terms of the CC BY-NC-SA 4.0, which permits copying, redistributing, remixing, transformation, and building upon the material in any medium so long as the original work is properly cited.

doi: 10.4108/ew.14509

*Corresponding author. Email: jfs20260612@163.com

1. Introduction

As the global energy transformation accelerates, a large amount of renewable energy has been connected to the power grid, encouraging the advancement of new power systems and the evolution of traditional ones [1]. Grid-Forming Energy Storage Converter (GFM-ESC), as the key interface equipment to achieve source-network coordinated control in new power systems, assumes the core functions of voltage and frequency support [2]. Compared with grid-connected converters that rely on phase-locked loops to synchronize the power grid, GFM-ESC simulates the power frequency characteristics of synchronous generators and is suitable for complex scenarios such as high-proportion new energy access and island operation [3]. However, GFM-ESC presents a variety of topologies in actual engineering applications, and different topologies have significant differences in wiring methods, component parameter configurations, and control coupling degrees [4]. Large disturbance scenarios include severe fluctuations in renewable energy power, transient impacts on the power grid, and island switching. Under these operating conditions, topological differences will lead to significant differentiation of system dynamic behavior [5]. Currently, the control strategy of GFM-ESC achieves dynamic response through multi-level control of power loop, voltage loop and current loop, but the impact of topology on system dynamic characteristics is ignored in existing modeling and control methods [6].

In the last few years, extensive research progress has been achieved in modeling and control methods for GFM-ESC. In terms of modeling, many scholars have established a variety of GFM-ESC kinetic models [7]. Wu Z et al. proposed a method for synchronous control of GFM-ESC and power grid. This approach built a new controller for grid-forming converters based on a stable dynamic model. The results showed that this method could reduce frequency deviation [8]. Zhang Z et al. proposed a dynamic modelling method for GFM-ESC in renewable energy power plants. The objective was to determine the ideal balance between the capacity of grid-forming and grid-following converters within the power plant. Results showed that this method performed more effectively in restoring synchronicity [9]. However, the above modeling studies are all based on a single fixed topology structure, without considering the essential differences in wiring methods and parameter configurations between different topologies such as direct hanging and string connection. Their model structures lack scalability for topological features and are difficult to generalize to large disturbance dynamic descriptions in multi-topology scenarios.

Regarding network control strategy, virtual synchronous generator control has become the mainstream technology route [10]. Pouresmaeil M et al. raised a control method for GFM-ESC based on virtual synchronous generator, which achieved over-current protection and system voltage support by coordinating voltage and current control. The results showed that this method could effectively limit the current and ensure high power quality [11]. Suvorov A et al. put forward a GFM-ESC control system grounded on virtual synchronous generator. The system coupled inertia and governor response to achieve multi-layer collaborative control of the power generation unit at the converter interface. The outcomes denoted that the system could improve the transient performance and damping characteristics [12]. Although virtual synchronous machine control has become mainstream, its fixed inertia coefficient and damping coefficient have response lag problems when dealing with large power fluctuations, and parameter tuning usually relies on empirical trial and error, lacking a mechanism for adaptive adjustment with the degree of disturbance, which limits the dynamic support capability under transient conditions.

In terms of robust control, H∞ robust control theory is broadly utilized in the converter control systems because of its good ability to suppress model uncertainty and external disturbances [13]. Martínez-Turégano J et al. proposed a GFM-ESC design method wtih H∞ control for high-voltage DC rectifier-connected wind power plants, and synthesized a robust controller by considering different operating modes. The outcomes demonstrated the performance of this method in enhancing the performance and robustness of the standard proportional resonant controller [14]. Rathnayake et al. suggested a second-order discrete-time controller design method with H_∞ control to achieve a smooth step response of the grid-forming inverter to power commands, thereby enhancing the provision of virtual inertia. The findings revealed that the controller outperformed the virtual synchronous generator controller in terms of tracking performance and virtual inertia provision [15]. However, the existing designs of H∞ controllers are based on fixed nominal models and do not incorporate changes in topology parameters into the constraints of the control law. When the topology parameters deviate, their robustness performance significantly decreases, and there is a lack of collaborative mechanisms with intelligent optimization algorithms to achieve online dynamic tuning of parameters.

Intelligent optimization methods, such as the Particle Swarm Optimization (PSO) algorithm and the genetic algorithm, are used to adjust the control parameters of mesh-type converters [16]. Çelebi M and Başçi A raised a GFM-ESC parameter optimization method grounded on PSO optimization, using a fractional-order proportional-integral controller to simulate a dual-active bridge series resonant converter. This method achieved the same optimal control parameters as the traditional algorithm [17]. Qi Y et al. put forward a GFM-ESC system optimization configuration method based on GA to cope with load uncertainty and renewable energy fluctuations by simultaneously optimizing the scale, location and operating features of the energy storage system. The results showed that this method could improve energy efficiency by 17.6% and reduce peak load impact by 22.3% [18].

In summary, existing research ignores topological differences and is difficult to characterize the large disturbance characteristics of multiple topologies. Robust control lacks the ability to dynamically adapt topological parameters and insufficient stability margin guarantee.

Therefore, the study proposes a robust stable control method for GFM-ESC under large disturbance scenarios. By establishing a large disturbance dynamic model of multi-topology GFM-ESC, a robust stable control method for topology adaptation is proposed to explore its performance under large disturbances and parameter perturbations. The novelty of this study is that topological features are embedded into the closed-loop control law rather than treated as external uncertainties, so that H∞ robust control can dynamically adapt to topological parameter variations. This differs from existing integrated converter control schemes, in which robust control, fuzzy adaptation, and optimization are typically combined without topological constraints in the control law. Here, the theoretical advance is the topology-adaptive robust stability condition derived from the perturbed state-space model, while fuzzy adaptation and improved PSO are used only as auxiliary online tuning mechanisms for inertia and damping.

2. Methodology

2.1. Construction of large-disturbance dynamics model for multi-topology GFM-ESC

GFM-ESC has various topological structures in new power systems, and different topologies have significant differences in wiring methods, component parameter configurations and control coupling levels [19]. It is difficult for existing modeling methods to accurately characterize the energy flow paths and stable boundary changes of multi-topology GFM-ESC under large disturbances. Therefore, a multi-topology GFM-ESC large perturbation dynamic model was constructed to quantify the impact of topological parameters on the system stability boundary. The topology diagram of GFM-ESC is shown in Fig.1.

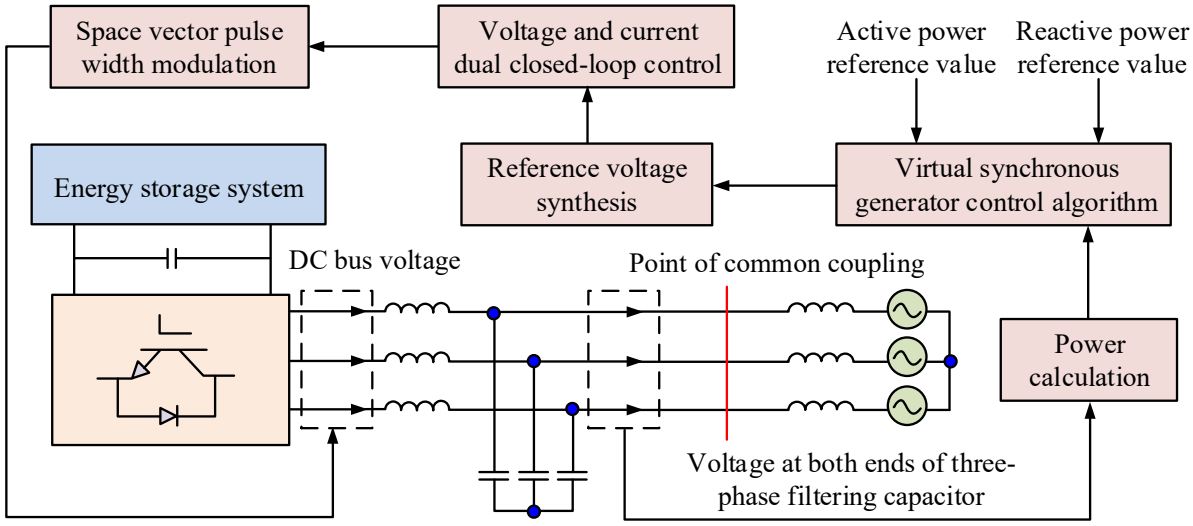


Figure 1. Schematic diagram of GFM-ESC topology

In Fig.1, the topology of GFM-ESC covers modules such as energy storage system, virtual synchronous generator control, power calculation, voltage and current double closed-loop control, and space vector pulse width modulation. This topology achieves grid-connected operation through reference voltage synthesis and power control. To quantify the influence of topological parameters on the system stability boundary, the study first analyzed the mapping relationship between the wiring topology, component parameters and the system state matrix. In constructing the dynamic model, the large perturbation swing Equation of its active power-frequency control is denoted in Equation (1).

$$P_{\text{ref}} - P_e - D_p(\omega - \omega_g) = J\omega_n \frac{d\omega}{dt} \quad (1)$$

In Equation (1), P_{ref} denotes the active power reference value. P_e means the electromagnetic active power output by GFM-ESC. D_p denotes the active power-frequency droop coefficient. ω and ω_g denote the virtual rotor Angular Frequency (AF) and the grid AF respectively. J and ω_n are virtual moment of inertia and rated AF respectively. After establishing the active power control response mechanism, to further realize the reasonable distribution of reactive power in the complex network, the study introduced a reactive power-voltage droop control loop. Its transient coupling process is shown in Equation (2).

$$E = E_n + \frac{1}{K_q s + 1}(Q_{\text{ref}} - Q_e) + K_v(U_{\text{ref}} - U_m) \quad (2)$$

In Equation (2), E denotes the internal potential amplitude. E_n denotes the rated internal potential amplitude. K_q means the reactive power-voltage droop integration time constant. s is the Laplacian operator. Q_{ref} and Q_e denote the reactive power reference value and the actual output reactive power respectively. K_v denotes the voltage droop coefficient. U_{ref} and U_m denote the grid connection point voltage reference value and actual amplitude respectively. To effectively overcome the electromagnetic interference caused by the system line coupling effect and improve the overall efficiency, the research introduces a voltage and current double closed-loop structure, as denoted in Fig.2.

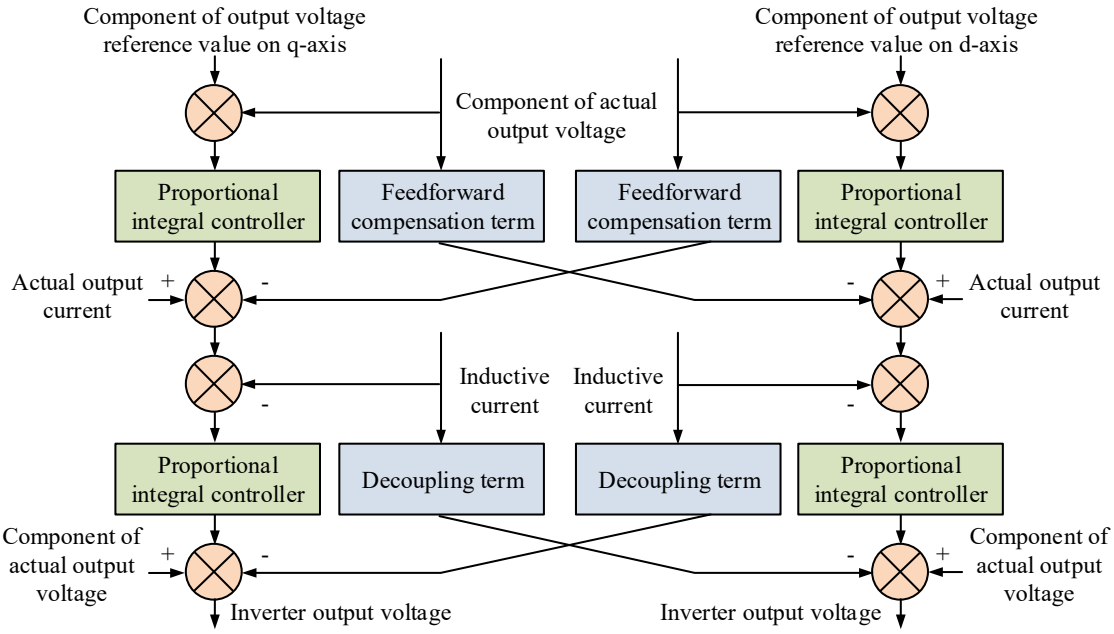


Figure 2. Schematic diagram of voltage and current dual closed-loop control

In Fig.2, the outer loop voltage control generates the current reference value through the proportional integral regulator. The inner loop current control is grounded on the proportional integral regulator, combining the inductor current decoupling term and the capacitor voltage feedforward compensation term to achieve fast and accurate current tracking. In precise control of the inner loop, the dynamic characteristics of the filter inductor current and capacitor voltage, which are based in the rotating coordinate system, can be expressed as a matrix, as shown in Equation (3).

$$\frac{d}{dt}\begin{bmatrix} i_{Ld} \\ i_{Lq} \end{bmatrix} = \begin{bmatrix} -R_f / L_f & \omega \\ -\omega & R_f / L_f \end{bmatrix}\begin{bmatrix} i_{Ld} \\ i_{Lq} \end{bmatrix} + \frac{1}{L_f}\begin{bmatrix} v_{id} & v_{cd} \\ v_{iq} & v_{cq} \end{bmatrix} \quad (3)$$

In Equation (3), i_{Ld} and i_{Lq} indicate the components of the filter inductor current on the d axis and the q axis. R_f denotes the equivalent series resistance of the filter inductor. L_f means the filter inductor value. v_{id} and v_{iq} are the components of the converter output voltage on the d axis and the q axis. v_{cd} and v_{cq} mean the components of the filter capacitor voltage on the d axis and q axis. To achieve accurate feedforward decoupling of the inner loop system state under large disturbance scenarios, a voltage and current double closed-loop proportional integral control law is studied and designed, as shown in Equation (4).

$$v^*_{dq} = K_{p,c}(i^*_{dq} - i_{dq}) + K_{i,c}\int (i^*_{dq} - i_{dq})dt + \omega L_f i_{qd} + v_{cdq} \quad (4)$$

In Equation (4), v^*_{dq} is the reference value of the converter output voltage. $K_{p,c}$ and $K_{i,c}$ are the current

loop proportional coefficient and integral coefficient. i^*_{dq} and i_{dq} are the current reference value and actual current respectively. v_{cdq} is the capacitor voltage feedforward term. To describe the changing rules of component parameters caused by multi-topological structures, a large perturbation generalized nonlinear state space model containing topological perturbation parameters is constructed, as shown in Equation (5).

$$\dot{\boldsymbol{x}}(t) = \boldsymbol{A}(\rho)\boldsymbol{x}(t) + \boldsymbol{B}(\rho)\boldsymbol{u}(t) + \boldsymbol{E}(\rho)\boldsymbol{w}(t) \tag{5}$$

In Equation (5), $\boldsymbol{x}(t)$ and $\dot{\boldsymbol{x}}(t)$ express the system state vector and the time derivative of the vector respectively. ρ indicates the topological perturbation parameter. $\boldsymbol{A}(\rho)$ and $\boldsymbol{B}(\rho)$ refer to the state matrix and input matrix. $\boldsymbol{u}(t)$ and $\boldsymbol{w}(t)$ denote the control input vector and external disturbance vector. $\boldsymbol{E}(\rho)$ stands for the perturbation input matrix. To clarify the physical meaning of topology perturbation parameters, the line impedance and filter parameters are defined as the perturbation variables for the direct-mounted topology, the series-connected inductances and capacitances as the coupling terms for the string-type topology, and the equivalent line impedance and coupling modes as the reduced-order parameters for the centralized topology. For the direct-mounted topology, the line impedance and filter parameters are mapped into the diagonal entries of $\boldsymbol{A}(\rho)$, while the coupling terms remain decoupled. For the string-type topology, the series-connected filter inductances and capacitances are aggregated into the off-diagonal coupling terms of $\boldsymbol{A}(\rho)$, and the state matrix exhibits a banded structure. For the centralized topology, the parallel branches are merged into a reduced-order state matrix, where the equivalent line impedance and coupling modes dominate the eigenvalue distribution. These topology-dependent mappings are explicitly embedded in $\boldsymbol{A}(\rho)$, $\boldsymbol{B}(\rho)$, and $\boldsymbol{E}(\rho)$, enabling the state matrix to reflect the structural differences among the three topologies. The line impedance was set to 0.1 p.u. and the filter inductance to 0.5 mH for the direct-mounted topology, while two series-connected inductances of 0.5 mH and a coupling capacitance of 50 μF were set for the string-type topology. The dominant eigenvalue of the direct-mounted topology was −18.6 + j12.4, whereas that of the string-type topology shifted to −9.7 + j21.8, indicating stronger coupling-induced oscillation. The transient energy peak increased from 0.42 p.u. to 0.68 p.u., which verifies that the proposed state-space model can mathematically distinguish different topologies.

To further improve the accuracy of state estimation for large-scale energy storage power plants, recent research progress on joint estimation of battery states has been incorporated into a dynamic modeling framework. An improved harmonic loss historical gating unit recovery method is adopted for the online joint estimation of the state of charge and energy state, to more accurately characterize the internal state of the energy storage system under large disturbances [20]. In addition, a novel square root unscented Kalman filtering strategy with full parameter online identification is introduced for power state assessment, achieving accurate evaluation of power capability under transient conditions [21]. Meanwhile, a critical review on improving hybrid deep learning modeling strategies is referenced to guide the selection of online state of charge estimation methods for large-scale energy storage systems [22]. After obtaining the generalized state space model, the transient energy function is constructed to evaluate the specific impact of topological parameters on the system's large disturbance stability boundary, as shown in Equation (6).

$$V(\boldsymbol{x}) = \frac{1}{2}\boldsymbol{x}^T\boldsymbol{P}\boldsymbol{x} + \int_0^t \widetilde{P}_e(\tau)d\tau \tag{6}$$

In Equation (6), $V(\boldsymbol{x})$ is the transient energy function. $\boldsymbol{x}$ means the system state vector. $\boldsymbol{P}$ means the positive definite moment of symmetry. $\widetilde{P}_e(\tau)$ is the electromagnetic power deviation. τ is the integral variable.

2.2 GFM-ESC robust stable control method based on fuzzy adaptive control and PSO

On the basis of establishing a multi-topology large disturbance dynamic model, to solve that fixed parameters in traditional control are difficult to adapt to large disturbances, a GFM-ESC robust stable control method based on fuzzy adaptive control and PSO algorithm is raised. This method derives the control law based on H∞ theory and aims to improve the system's ability to suppress parameter perturbations and large disturbances. To ensure that the suppression effect is still effective under extreme working conditions, for the set disturbance attenuation degree, the H∞ robust performance index of the closed-loop system must satisfy the constraints as shown in Equation (7).

$$\int(\boldsymbol{z}^T\boldsymbol{Q}\boldsymbol{z} + \boldsymbol{u}^T\boldsymbol{R}_u)dt \le \gamma^2\int_0^\infty \boldsymbol{w}^T\boldsymbol{w}dt \tag{7}$$

In Equation (7), $\boldsymbol{z}$ is the performance output vector. $\boldsymbol{Q}$ and $\boldsymbol{R}$ denote the state and the control weighting matrices. γ is the disturbance attenuation degree. Then, the Lyapunov theory is used to study the sufficient conditions to ensure that the closed-loop system state matrix maintains global asymptotic stability characteristics, and its positive definite matrix satisfies [23]. The linear matrix inequality used for controller synthesis is shown in equation (8).

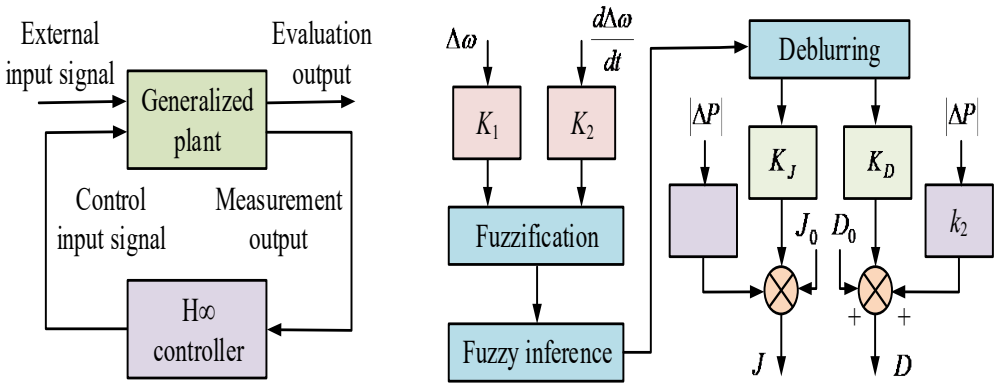
$$\begin{bmatrix} \boldsymbol{P}+\boldsymbol{PA}+\boldsymbol{Q} & \boldsymbol{PE} & \boldsymbol{PB} \\ \boldsymbol{E}^T\boldsymbol{P} & -y^2 I & 0 \\ B^T\boldsymbol{P} & 0 & -\boldsymbol{R} \end{bmatrix} < 0 \quad (8)$$

In Equation (8), $\boldsymbol{P}$ is a positive definite symmetric matrix. The state weighting matrix and control weighting matrix are defined as $\boldsymbol{Q}=\mathrm{diag}(q_1,q_2,\ldots,q_n)>0$ and $\boldsymbol{R}=\mathrm{diag}(r_1,r_2,\ldots,r_m)>0$, respectively, where q_n and r_m are selected based on the relative importance of the state variables and control inputs. The disturbance attenuation index γ is selected within the feasible range $\gamma\in(0,\gamma_{\max}]$, where $\gamma_{\max}$ is determined by the existence conditions of the LMI positive definite solution $\boldsymbol{P}$. When $\boldsymbol{Q}>0$, $\boldsymbol{R}>0$, and γ satisfy the bounded real lemma condition, the LMI constraint is feasible, with parameter ranges of $0.1\le q_n\le 10$, $0.01\le r_m\le 1$, and $0.1\le\gamma\le 1.0$, respectively. The generalized controlled object is defined as the interconnected structure of a multi topology state space model and performance output channels, where the performance output is represented as $z=\boldsymbol{Q}x+\boldsymbol{R}u$, and $\boldsymbol{Q}$ and $\boldsymbol{R}$ are positive definite diagonal weighted matrices. The controller synthesis is expressed as an LMI feasibility problem, whose positive definite solution P ensures both the H ∞ performance index and the asymptotic stability of the closed-loop system.

To overcome the defect of dynamic response hysteresis caused by fixed parameters, an inertia and damping optimization strategy based on fuzzy adaptive control is put forward. The dynamic update law of its virtual moment of inertia is shown in Equation (9).

$$J(t)=J_0+K_J\Delta\omega(t)\cdot\mathrm{sgn}(\frac{d\Delta\omega}{dt})+\Delta J_{\text{fuzzy}} \quad (9)$$

In Equation (9), $J(t)$ is the time-varying virtual moment of inertia. J_0 denotes the virtual moment of inertia reference value. K_J means the adaptive adjustment gain coefficient. $\Delta\omega(t)$ is the frequency deviation. $\mathrm{sgn}(\frac{d\Delta\omega}{dt})$ is the sign function of the frequency deviation change rate. ΔJ_{fuzzy} is the inertia adjustment amount output by the fuzzy controller. The schematic diagram of H∞ robust control and fuzzy adaptive control strategy is shown in Fig.3.



(a) H∞ robust control (b) Schematic diagram of fuzzy adaptive control strategy

Figure 3. Schematic diagram of H∞ robust control and fuzzy adaptive control strategy

Fig. 3(a) shows the H∞ robust control structure. The generalized controlled object and the H∞ controller form a closed loop to effectively suppress the disturbance input and ensure that the system meets the robust performance index under parameter perturbations and large disturbances. Fig. 3(b) takes the frequency deviation and its change rate as input, and after fuzzification, fuzzy reasoning and defuzzification, the power adjustment amount is output, and the virtual inertia and damping coefficient are dynamically updated. To suppress the high-frequency oscillation problem caused by sudden changes in large disturbance power, a damping fuzzy optimization mechanism is introduced, and the update law of the adaptive damping coefficient is shown in Equation (10).

$$=D_0+K_D\left|\frac{d\Delta\omega}{dt}\right|+\Delta D_{\text{fuzzy}} \quad (10)$$

In Equation (10), $D(t)$ denotes the time-varying adaptive damping coefficient. D_0 is the base value of damping coefficient. K_D is the damping adaptive gain coefficient. $\left|\frac{d\Delta\omega}{dt}\right|$ is the absolute value of the frequency deviation change rate. ΔD_{fuzzy} is the damping adjustment amount output by the fuzzy controller. To avoid the system falling into local extreme values, the improved PSO algorithm is introduced to perform global optimization of basic control parameters. The particle velocity update of the improved PSO algorithm in the k-th iteration is shown in Equation (11) [24].

$$v_{ij}^{(k+1)} = w(k)v_{ij}^{(k)} + c_1 r_1 (p_{ij}^{(k)} - x_{ij}^{(k)}) + c_2 r_2 (g_j^{(k)} - x_{ij}^{(k)}) \quad (11)$$

In Equation (11), $v_{ij}^{(k+1)}$ is the speed of the i-th particle in the j-th dimension and the $k+1$-th iteration. $w(k)$ means the inertia weight at the k-th iteration. c_1 and c_2 indicate individual and social learning factors. r_1 and r_2 indicate random numbers in the interval [0,1]. $p_{ij}^{(k)}$ means the historical optimal position of the i-th particle in the j-th dimension. $x_{ij}^{(k)}$ means the current position of the particle in the j-th dimension and the k-th iteration. $g_j^{(k)}$ means the global optimal position of the group in the j-th dimension. Finally, to ensure that the optimization algorithm has a broad search space in the early stage of iteration and can perform high-precision local development in the later stage, the improved PSO algorithm adopts a dynamic adjustment mechanism. The calculation of the nonlinear decrease of its core inertia weight is denoted in Equation (12).

$$w(k) = w_{\max} - (\frac{w_{\max} - w_{\min}}{k_{\max}})k \quad (12)$$

In Equation (12), $w_{\max}$ and $w_{\min}$ express the max and mini values of the inertia weight. $k_{\max}$ refers to the max amount of iterations. The fitness function is defined as $F = \alpha_1 \cdot \text{MFD} + \alpha_2 \cdot T_{\text{rec}} + \alpha_3 \cdot E_{\text{ss}}$, where α_1, α_2, and α_3 are weight coefficients, taken as 0.4, 0.3, and 0.3, respectively. The particle population size is set to 30 and the maximum number of iterations is set to 100. The stopping rule is to terminate the iteration when the fitness improvement is less than 10-4 for 10 consecutive iterations or when the maximum number of iterations is reached. The fuzzy membership function adopts a triangular function and is divided into five language levels (NB, NS, ZO, PS, PB). The fuzzy rule table contains 25 rules. The flow chart of the improved PSO algorithm is denoted in Fig.4.

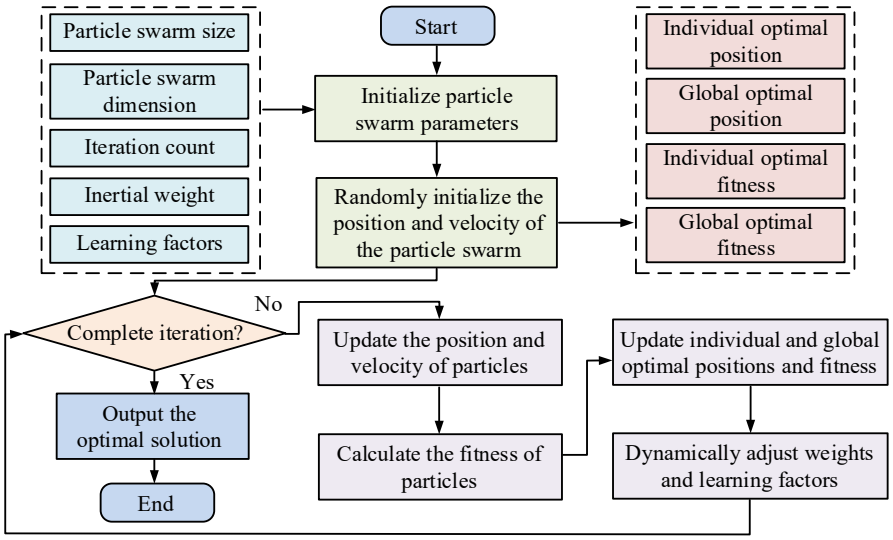


Figure 4. Process diagram for improved PSO algorithm

On the basis of the improved PSO algorithm, the optimized parameters are used as initial values and put into the fuzzy adaptive H∞ robust controller. The controller detects the system frequency deviation and its change rate in

real time, dynamically adjusts the virtual inertia and damping coefficient through fuzzy reasoning, and combines the H∞ control law to suppress the effects of large disturbances and parameter perturbations, achieving robust and stable operation of GFM-ESC in multi-topology scenarios. The overall architecture of the robust stability control system for multi-topology GFM-ESC is shown in Fig.5.

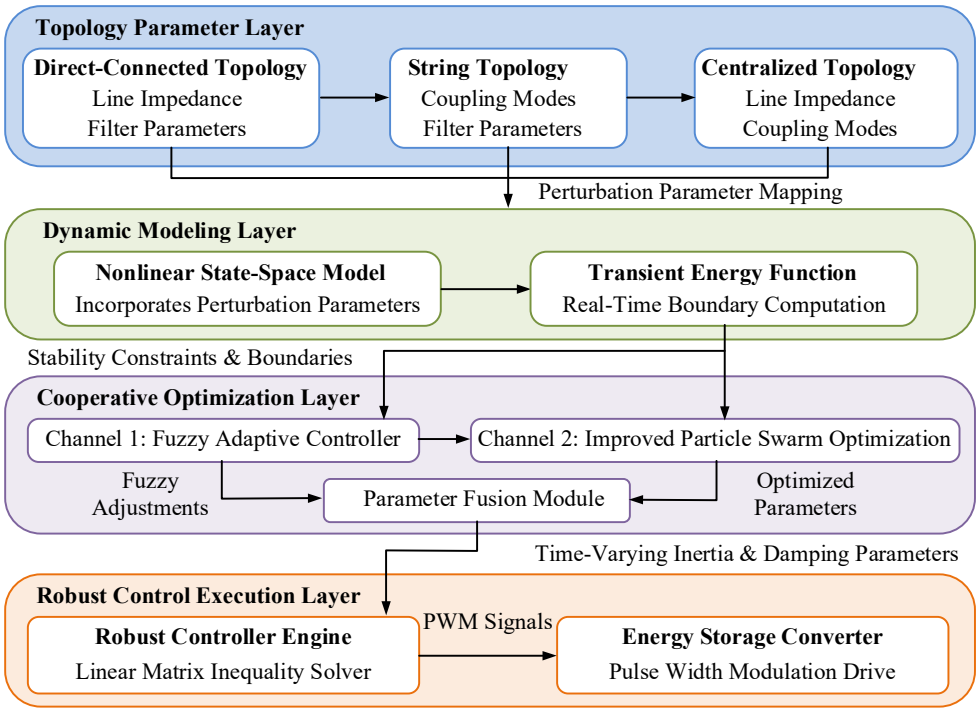


Figure 5. Overall architecture of robust stability control system for multi-topology networked energy storage inverters

Fig.5 shows the overall architecture of the robust stability control system for multi-topology GFM-ESC, which includes four modules: topology parameter layer, dynamic modeling layer, collaborative optimization layer, and robust control execution layer. The topological parameters are input into the dynamic modeling layer through perturbation mapping, generating a nonlinear state space model containing transient energy functions, and outputting stability constraints to the collaborative optimization layer. In the collaborative optimization layer, the fuzzy adaptive controller and improved PSO algorithm are optimized in parallel, integrating to generate time-varying inertia and damping parameters for the robust controller to solve linear matrix inequalities, and finally outputting PWM signals to drive the inverter, forming a closed-loop control link.

3. Results and Analysis

3.1. Small signal analysis of multi-topology GFM-ESC

To test the performance of the developed multi-topology dynamic model and robust control method, the study simulated and evaluated the dynamic response features of GFM-ESC under power command and load mutation conditions. The simulation was built based on the MATLAB/Simulink, and the simulation time was set to 1.2s. The initial power command was 10kW. At 0.5s, the power command suddenly increased from 10kW to 40kW, and then at 1.0s, the power command suddenly decreased to 10kW. For the load mutation condition, the initial power was 10kW, a load of 20kW was added at 0.5s, and the load of 20kW was removed at 1.0s. The study compared the proposed control method with fixed parameters and fuzzy adaptive control method. The parameter settings of the simulation model are denoted in Table 1.

Table 1. Main parameter settings for simulation models

Parameters	Values	Parameters	Values
Rated power	500kW	Virtual inertia reference value	0.8kg·m2
Rated voltage	380V	Damping coefficient reference value	20p.u.
Rated frequency	50Hz	Active power-frequency droop coefficient	0.02p.u.
DC-link voltage	800V	Voltage droop coefficient	0.05p.u.
Filter inductance	0.5mH	Current loop proportional gain	0.8
Filter capacitance	50μF	Current loop integral gain	50
Switching frequency	40kHz	H∞ disturbance attenuation level	0.5

The study analyzed the dynamic power response features of different methods under the conditions of power command and load mutation. The findings are denoted in Fig.6.

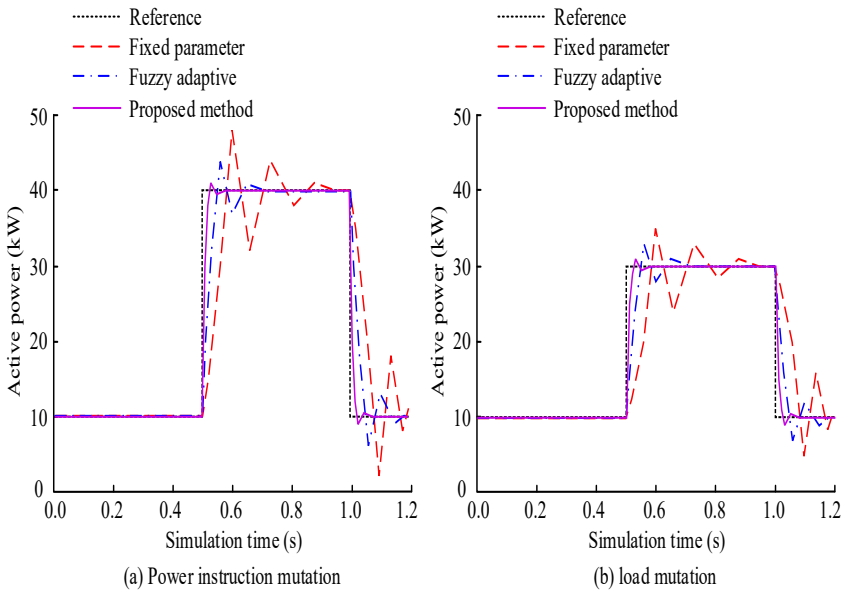


Figure 6. Active power response curves of the fixed-parameter, fuzzy adaptive, and proposed methods under sudden power command changes and sudden load changes

From Fig.6(a), under the condition of sudden change in power command and the simulation time was 0.6s, the active power of the fixed parameter and fuzzy adaptive control methods were 47.8kW and 36.5kW respectively, and the active power of the proposed method was 40.0kW, which was closer to the reference value. When the simulation time was 1.1s, the active powers of the three control methods were 2.1kW, 13.4kW and 10.0kW respectively. In Fig.6(b), under the condition of sudden load change and the simulation time was 0.6s, the active powers of the three control methods were 34.8kW, 28.2kW and 30.0kW respectively. The results indicate that the developed method can effectively improve the dynamic tracking accuracy and

disturbance suppression capability of active power under both mutation conditions.

The study further analyzed the frequency response characteristics of different methods under the conditions of sudden changes in power command and load. The outcomes are indicated in Fig.7.

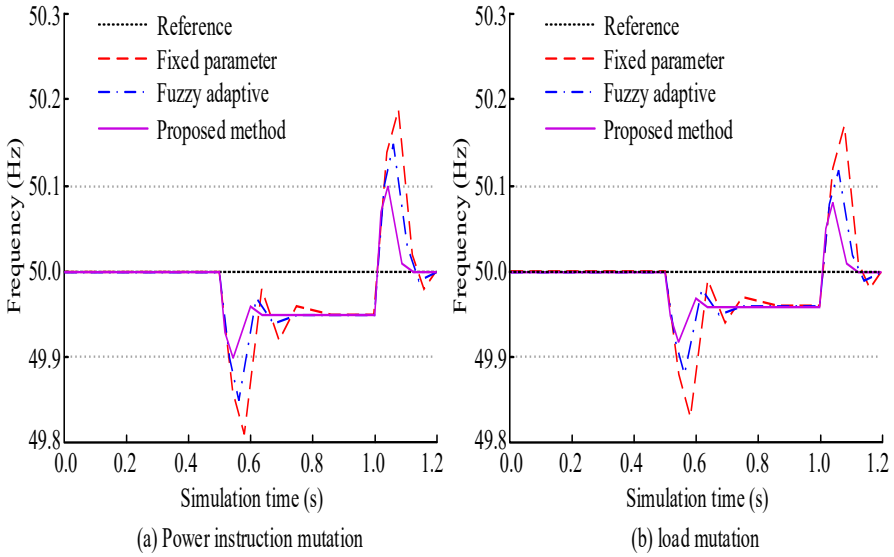


Figure 7. Frequency response curves of the fixed-parameter, fuzzy adaptive, and proposed methods under sudden power command changes and sudden load changes

In Fig.7(a), under the condition of sudden change of power command, when the simulation time reached 1.09s, the fixed parameter control method reached a peak value of 50.18Hz. When the time was 1.05s, the fuzzy adaptive control method had a peak value of 50.14Hz. In comparison, the proposed method reached a peak value of 50.10Hz when the simulation time was 1.03s. In Fig.7(b), under the condition of sudden load change, when the simulation time reached 1.08s, 1.06s and 1.04s respectively, the fixed parameters, fuzzy adaptive and proposed control method had peak values, which were 50.16Hz, 50.13Hz and 50.08Hz respectively. The proposed method can effectively suppress frequency fluctuations and improve the frequency support capability and transient stability of the system.

To prove the dynamic adjustment capability of the developed method, the virtual moment of inertia and adaptive damping coefficient of different methods were analyzed under the conditions of sudden changes in power command and load. The findings are denoted in Fig.8.

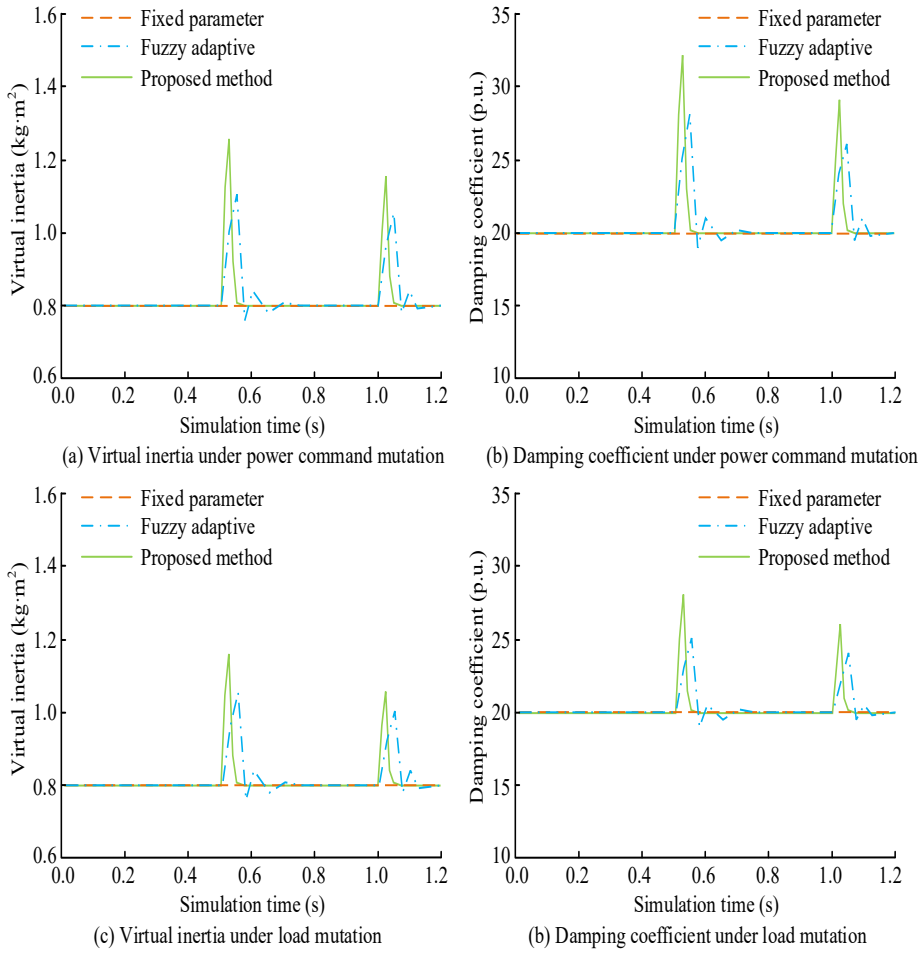


Figure 8. Curves of the virtual moment of inertia and the adaptive damping coefficient of the fixed-parameter, fuzzy adaptive, and proposed methods under sudden power command changes and sudden load changes

In Fig.8(a) and Fig.8(b), under the condition of power command mutation, the virtual inertia of the fixed parameter control method was always 0.80kg·m2, and the adaptive damping coefficient was always 20.0p.u. The peak values of virtual inertia and adaptive damping coefficient of the fuzzy adaptive control method were 1.12kg·m2 and 27.81p.u. respectively. The peak values of the proposed method were 1.25kg·m2 and 32.62p.u. respectively, and the response time was faster. In Fig.8(c) and Fig.8(d), under the load mutation condition, the virtual inertia peaks of the fuzzy adaptive and proposed methods were 1.04kg·m2 and 1.17kg·m2 respectively, and the adaptive damping coefficients were 25.02p.u. and 28.05p.u. respectively, and the response time of the developed method was faster. The findings reveal that the developed method can dynamically adjust the inertia and damping according to the degree of disturbance and achieve better transient regulation capability.

3.2. Large disturbance simulation results of GFM-ESC robust stability control

To test the effectiveness of the GFM-ESC robust stability control method in large disturbance scenarios, the study carried out large disturbance simulation analysis on the MATLAB/Simulink. The simulation model ran in island mode, the simulation time was 1.2s, the initial power was 10kW, and the load was 6kVa. When the time was 0.4s, there was a sudden increase of 20kW. The study analyzed the response characteristics of active power, reactive power and frequency of different methods in the island mode. The results are shown in Fig.9.

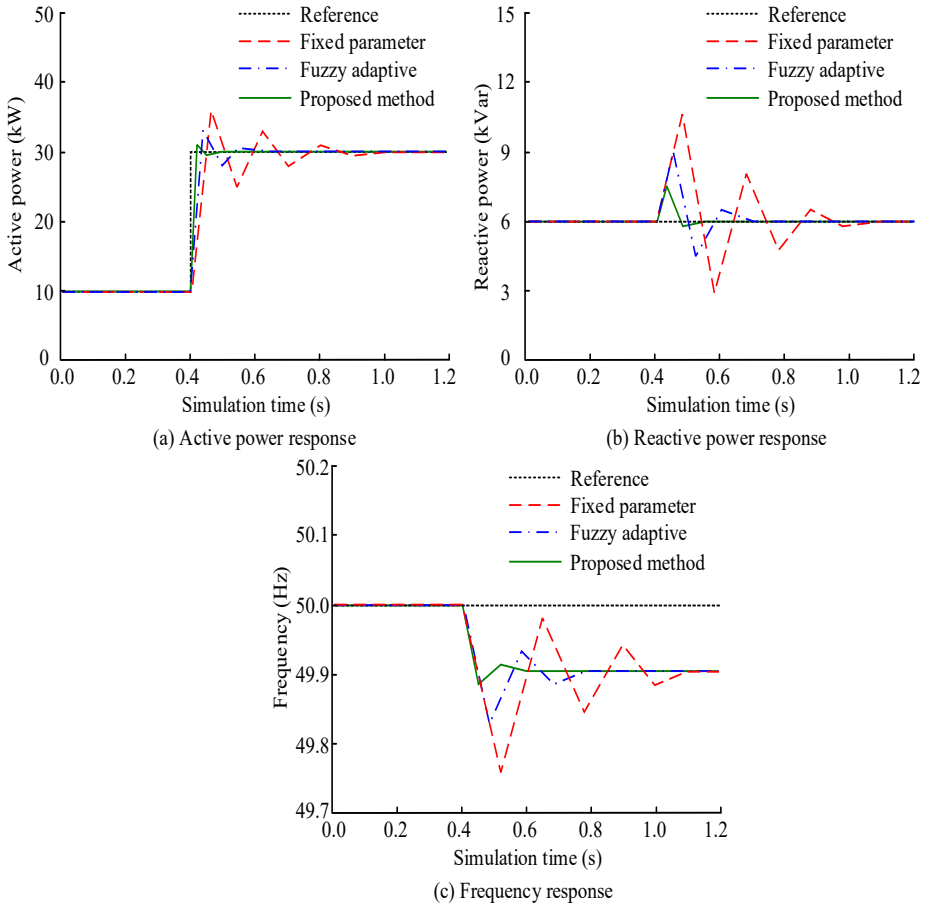


Figure 9. Active power, reactive power, and frequency response curves of the fixed-parameter, fuzzy adaptive, and proposed method in islanding mode

In Fig.9(a), when the simulation time was 0.50s, the active power of the proposed method reached 30.0kW. When the simulation time reached 0.63s and 1.02s respectively, the active power of the fixed parameter and fuzzy adaptive control methods reached 30.0kW. In Fig.9(b), when the simulation times were 1.08s, 0.70s and 0.55s respectively, the reactive power of fixed parameters, fuzzy adaptive and the developed method reached 6kVa. In Fig.9(c), when the simulation times were 1.10s, 0.78s and 0.60s respectively, the frequencies of the three control methods all reached 49.90Hz. The results indicate that the developed method has a faster response recovery time. The frequency does not reach 50Hz. The reason is that there is a slight steady-state deviation in the system after the load changes in island mode.

The study conducted a comparative analysis on the Maximum Frequency Deviation (MFD), frequency recovery time, steady-state error and robust stability margin of different methods under no perturbation conditions and 15% perturbation of topological parameters. The findings are denoted in Table 2.

Table 2. Performance comparison of different control methods under large disturbance scenarios with 15% topological parameter perturbations

Working condition	Evaluation Indicator	Fixed parameter	Fuzzy adaptive	Proposed method
No perturbation condition	MFD (Hz)	1.24	0.91	0.68
	Frequency recovery time (s)	1.85	1.23	0.94
	Steady state error (kW)	8.20	4.50	2.10
	Stability margin	0.82	1.13	1.16

Operating condition with topological parameter perturbation of 15%	MFD (Hz)	1.67	1.18	0.72
	Frequency recovery time (s)	2.43	1.56	1.02
	Steady state error (kW)	12.50	6.80	2.40
	Stability margin	0.61	0.95	1.08

In Table 2, under non-perturbation conditions, the MFD of the proposed method was 0.68 Hz, which was 45.2% and 25.3% lower than the fixed parameter method and the fuzzy adaptive method. The frequency recovery time was 0.94 s, the steady-state error was 2.10 kW, and the stability margin reached 1.16. Compared with the fixed parameter method, the stability margin was increased by 42%. Under the condition of 15% topological parameter perturbation, the MFD of the proposed method was 0.72 Hz, and the stability margin was 1.08. The results indicate that the developed method can still maintain excellent robustness and stability margin under parameter perturbation.

To further verify the adaptability of the proposed method under different disturbance conditions, a multi-factor sensitivity test was added, and the results are shown in Table 3. According to Table 3, as the disturbance amplitude increased from 10 kW to 30 kW, the MFD increased from 0.42 Hz to 0.95 Hz, and the stability margin decreased from 1.28 to 1.04. When the impedance of the power grid increased from 0.1 p.u. to 0.5 p.u., the frequency recovery time was extended from 0.78 s to 1.18 s, and the stability margin dropped to 1.09. When the load type changed from resistive to nonlinear, the steady-state error increased from 1.88 kW to 2.68 kW, and the stability margin decreased to 1.06. When the fluctuation of new energy power increased from 10% to 30%, the MFD increased from 0.52 Hz to 0.91 Hz, and the stability margin decreased to 1.05. Although various indicators deteriorate with increasing disturbance, the proposed method has a stability margin greater than 1.0 under all testing conditions, indicating that it still has good adaptability and robust stability in large disturbance scenarios.

Table 3. Sensitivity test results of the proposed method under different disturbance scenarios

Sensitivity Factor	Variation Range	MFD (Hz)	Frequency Recovery Time (s)	Steady-State Error (kW)	Stability Margin
Disturbance magnitude	10 kW	0.42	0.58	1.2	1.28
	20 kW	0.68	0.94	2.1	1.16
	30 kW	0.95	1.32	3.05	1.04
Disturbance timing	0.3 s	0.61	0.86	1.95	1.19
	0.5 s	0.68	0.94	2.1	1.16
	0.7 s	0.74	1.05	2.28	1.12
Grid impedance	0.1 p.u.	0.55	0.78	1.72	1.22
	0.3 p.u.	0.68	0.94	2.1	1.16
	0.5 p.u.	0.83	1.18	2.56	1.09
Load type	Resistive	0.6	0.84	1.88	1.2
	Inductive	0.72	1.02	2.24	1.13
	Nonlinear	0.88	1.26	2.68	1.06
Renewable power fluctuation	0.1	0.52	0.72	1.62	1.24
	0.2	0.68	0.94	2.1	1.16
	0.3	0.91	1.28	2.92	1.05

To further quantify the individual contributions of each component in the proposed hybrid strategy, ablation comparative experiments were conducted on individual H ∞ control, H ∞+fuzzy adaptive control, H ∞+improved PSO,

and the entire proposed method under the same large disturbance conditions. The results are shown in Table 4. According to Table 4, the stability margin of H ∞ control alone was only 0.92, and the MFD was 1.15 Hz, indicating that robust control alone was difficult to guarantee large disturbance stability. After introducing fuzzy adaptive control, the stability margin increased to 1.05, the MFD decreased to 0.91 Hz, and the frequency recovery time was shortened to 1.24 seconds, indicating that the adaptive adjustment of inertia and damping effectively suppressed frequency fluctuations. After introducing the improved PSO, the stability margin further increased to 1.09 and the steady-state error decreased to 3.5 kW. The fully proposed method performed the best, with MFD reduced to 0.68 Hz, recovery time only 0.94 s, steady-state error reduced to 2.1 kW, and stability margin reached 1.16, which was 26.1% higher than the individual H ∞ control. This confirms that the three complement each other and the combination strategy improves significantly.

Table 4. Ablation study results of different control schemes under large disturbance scenarios

Control Scheme	MFD (Hz)	Frequency Recovery Time (s)	Steady-State Error (kW)	Stability Margin
H∞ alone	1.15	1.62	5.8	0.92
H∞ + Fuzzy Adaptive	0.91	1.24	3.9	1.05
H∞ + Improved PSO	0.86	1.18	3.5	1.09
Complete Proposed Method	0.68	0.94	2.1	1.16

4. Conclusion

Aiming at the stability control of grid-forming energy storage converters under multi-topology structures and large disturbance scenarios, this study established a large-disturbance dynamic model embedded with topological characteristics. On this basis, a robust stability control method combining H∞ robust control and fuzzy adaptive PSO optimization was proposed. Small signal analysis showed that the proposed method reduced the dynamic tracking error of active power under sudden changes in power command and load, and its frequency fluctuation suppression capability was better than fixed parameters and fuzzy adaptive methods. The simulation results of large disturbance island showed that when the simulation time was 0.50s, 0.55s and 0.60s respectively, the active power, reactive power and frequency of the proposed method reached constant, and its response time was better than the comparative method. Under non-perturbation conditions, the stability margin was increased to 1.16, and the MFD was minimized to 0.68 Hz. Under 15% topological parameter perturbation, the stability margin still remained 1.08, and the MFD was 0.72 Hz. The results indicate that the developed method has excellent disturbance suppression capability and robust stability margin. The limitation of this study is that it did not consider engineering factors such as multi-machine parallel connection and communication delay. Future research will conduct hardware-in-the-loop experiments and explore data-driven adaptive robust control strategies.

Acknowledgments

This work was supported by the project: Key-Area Research and Development Program of Guangdong Province. Project Number: 2023B0909030001.

References

[1] Liu Y, Chen Y, Xin H, Tu J, Zhang L, Song M, and Zhu J. System strength constrained grid-forming energy storage planning in renewable power systems. IEEE Transactions on Sustainable Energy. 2024; 16(2): 981-994.

[2] Alshahrani S, Khan K, Abido M, and Khalid M. Grid-forming converter and stability aspects of renewable-based low-inertia power networks: Modern trends and challenges. Arabian Journal for Science and Engineering. 2024; 49(5): 6187-6216.

[3] Wu X, Wu S, Wang F, Wei C, Li R, Jiang X, and Cai X. Grid-forming control and experimental validation for high voltage transformerless battery energy storage system. IEEE Transactions on Power Electronics. 2024; 40(4): 4889-4901.

[4] Zhao F, Wang X, and Zhu T. Power dynamic decoupling control of grid-forming converter in stiff grid. IEEE Transactions on Power Electronics. 2022; 37(8): 9073-9088.

[5] Favuzza S, Musca R, and Zizzo G. Comparative modeling and analysis of EMT and phasor RMS grid-forming converters under different power system dynamics. IEEE Transactions on Industry Applications. 2023; 60(2): 3613-3624.

[6] Chen M, Zhou D, Tayyebi A, Prieto-Araujo E, Dörfler F, and Blaabjerg F. On power control of grid-forming converters: Modeling, controllability, and full-state feedback design. IEEE Transactions on Sustainable Energy. 2023; 15(1): 68-80.

[7] Zhang K, Shi M, Chen X, Shao D, Xu Y, and Chen Y. Interaction modeling and stability analysis of grid-forming energy storage system based on SISO transfer functions. IEEE Transactions on Sustainable Energy. 2024; 16(1): 573-587.
[8] Wu Z, Zhang M, Fan B, Shi Y, and Guan X. Deep synchronization control of grid-forming converters: A reinforcement learning approach. IEEE/CAA Journal of Automatica Sinica. 2025; 12(1): 273-275.
[9] Zhang Z, Schuerhuber R, Fickert L, and Chen G. Dynamic modelling and equilibrium manifold of multi-converter systems: A study on grid-forming and grid-following converters in renewable energy power plants. IET Renewable Power Generation. 2024; 18(15): 3253-3267.
[10] Elshenawy MA, Radwan A, and Mohamed YARI. Unified sequence impedance models of synchronous generator- and virtual oscillator-based grid-forming converters. IEEE Transactions on Power Delivery. 2023; 39(1): 56-70.
[11] Pouresmaeil M, Sangrody R, Taheri S, Montesinos-Miracle D, and Pouresmaeil E. Enhancing fault ride through capability of grid-forming virtual synchronous generators using model predictive control. IEEE Journal of Emerging and Selected Topics in Industrial Electronics. 2024; 5(3): 1192-1203.
[12] Suvorov A, Askarov A, and Kievets A. A freely configurable structure of virtual synchronous generator for grid-forming converters. Electrical Engineering. 2023; 105(3): 1331-1345.
[13] Ali AJ, Abbas HH, and Bevrani H. Comparative analysis of H2 and H∞ robust control design approaches for dynamic control systems. Journal of Engineering. 2023; 29(08): 1-15.
[14] Martínez-Turégano J, Sala A, and Blasco-Gimenez R. Grid forming H∞ control for HVDC diode rectifier-connected wind power plants. CSEE Journal of Power and Energy Systems. 2023; 10(6): 2384-2397.
[15] Rathnayake DB, Me SP, Razzaghi R, and Bahrani B. H∞-based control design for grid-forming inverters with enhanced damping and virtual inertia. IEEE Journal of Emerging and Selected Topics in Power Electronics. 2022; 11(2): 2311-2325.
[16] Hossain MI, Anonto HZ, Shufian A, Pathik BB, Mannan MA, Rashid A, and Biswas P. Enhancing microgrid resilience through integrated grid-forming and grid-following inverter strategies for solar PV battery control and fault ride-through. Scientific Reports. 2025; 15(1): 40078-40106.
[17] Çelebi M and Başçi A. Parameter optimization of bidirectional three-phase DC-AC power inverter by an improved particle swarm optimization based fractional order PI controller for the grid forming operation. International Journal of Engineering Technologies IJET. 2022; 8(1): 25-30.
[18] Qi Y, Che Y, Liu L, Ni J, and Zhang S. Optimization configuration method for grid-side grid-forming energy storage system based on genetic algorithm. Energy Engineering: Journal of the Association of Energy Engineers. 2025; 122(10): 3999-4017.
[19] Teng Y, Deng W, Pei W, Li Y, Dingv L, and Ye H. Review on grid-forming converter control methods in high-proportion renewable energy power systems. Global Energy Interconnection. 2022; 5(3): 328-342.
[20] Wang S, Wei J, Zhang L, Li H, Fernandez C, and Blaabjerg F. Improved harmonic loss-history gated unit recycling for online state of charge and state of energy co-estimation of lithium-ion batteries for large-scale energy storage stations. Energy. 2025; 340: 139225.
[21] Wang S, Dang Q, Gao Z, Li B, Fernandez C, and Blaabjerg F. An innovative square root-untraced Kalman filtering strategy with full-parameter online identification for state of power evaluation of lithium-ion batteries. Journal of Energy Storage. 2024; 104: 114555.
[22] Wang S, Hu B, Zhang Q, Dang Q, and Fernandez C. Critical review on improved hybrid deep learning modeling strategies for online battery state of charge estimation in large-scale energy storage systems. Journal of Power Sources. 2026; 673: 239714.
[23] Shen C, Gu W, Shen X, and Xu Y. Lyapunov method-based coherent aggregation of grid-forming converters for transient stability equivalents. IEEE Transactions on Smart Grid. 2025; 16(2): 1462-1479.
[24] Zhu N, Hu P, Jiang C, Yu Y, and Jiang D. Comparative analysis and optimal allocation of virtual inertia from grid-forming and grid-following controlled ESSs. IET Renewable Power Generation. 2024; 18(14): 2416-2429.